Geoscience Frontiers 11 (2020) 1345–1352

Contents lists available at ScienceDirect

Geoscience Frontiers

journal homepage: www.elsevier.com/locate/gsf

Research Paper

Astronomical time scale of the Turonian constrained by multiple paleoclimate proxies

Chao Ma[a,*], Mingsong Li[b]

[a] Department of Computer Science, University of Idaho, Moscow, ID, 83843, USA
[b] Department of Geosciences, The Pennsylvania State University, University Park, PA, 16802, USA

ARTICLE INFO

Handling Editor: Wenjiao Xiao

Keywords:
Astrochronology
Astronomical time scale
Uncertainty
Cretaceous
Turonian
Demerara rise

ABSTRACT

One of the clocks that record the Earth history is (quasi-) periodic astronomical cycles. These cycles influence the climate that can be ultimately stored in sedimentary rocks. By cracking these (quasi-) periodic sedimentation signals, high resolution astronomical time scale (ATS) can be obtained. Paleoclimate proxies are widely used to extract astronomical cycles. However different proxies may respond differently to astronomical signals and non-astronomical noises including tectonics, diagenesis, and measurement error among others. Astronomical time scale constructed based on a single proxy where its signal-to-noise ratio is low may have uncertainty that is difficult to evaluate but can be revealed by utilizing other proxies. Here, we test eight astronomical age models using two astrochronological methods from four paleoclimate proxies (i.e., color reflection L* and b*, natural gamma radiation, and bulk density) from the Turonian to the Coniacian of the Cretaceous Period at the Demerara Rise in the equatorial Atlantic. The two astrochronological methods are time calibration using long eccentricity bandpass filtering (E1 bandpass) and tracking the long eccentricity from evolutive harmonic analysis (tracking EHA). The statistical mean and standard deviation of four age models from the four proxies are calculated to construct one integrated age model with age uncertainty in each method. Results demonstrate that extracting astronomical signals from multiple paleoclimate proxies is a valid method to estimate age model uncertainties. Anchored at the Cenomanian/Turonian boundary with an age of 93.9 ± 0.15 Ma from biostratigraphy, the ages for CC11/CC12 (calcareous nannofossil zones), Turonian/Coniacian (CC12/CC13), CC13/CC14, and Coniacian/Santonian boundaries are 91.25 ± 0.20 Ma, 89.87 ± 0.20 Ma, 86.36 ± 0.33 Ma, and 86.03 ± 0.32 Ma in E1 bandpass method, compared with 91.17 ± 0.36 Ma, 89.74 ± 0.38 Ma, 86.13 ± 1.31 Ma, and 85.80 ± 1.33 Ma respectively in tracking EHA method. These results are consistent with previous studies within error and provide a reliable estimation of uncertainties of the ages.

1. Introduction

Rhythmic sedimentary rocks that record astronomical cycles (i.e., orbital eccentricity, obliquity and precession of the Earth) can be used as a high-resolution ruler measuring the geological time scale (Gradstein et al., 2012; Ma et al., 2014; Eldrett et al., 2015a; Hinnov, 2018). The study of the astronomical cycles in sedimentary sequences is called astrochronology while the time scale constructed from astrochronology is called astronomical time scale (Hinnov, 2018). Uncertainties associated with astronomical time scale has been considered in recent studies (Kuiper et al., 2008; Meyers et al., 2012; Westerhold et al., 2012; Sageman et al., 2014; Li et al., 2016; Ma et al., 2017, 2019). Meyers et al. (2012) applied Bayesian method to constrain the uncertainty of astrochronology and radioisotopic ages of ash beds in the mid-Cretaceous. Uncertainties of astronomical time scale in the upper Cretaceous from Sageman et al. (2014) considered the age uncertainty derived from biostratigraphic and lithostratigraphic correlation. De Vleeschouwer and Parnell (2014) estimated age uncertainty for the Devonian by applying Bayesian method to astrochronology and radioisotopic geochronology. Ma et al. (2017a) evaluated the age uncertainty derived from the radioisotopic dating and uncertainty associated with different ash beds as anchors in astrochronology for upper Cretaceous strata. All these studies rely on results from single paleoclimate proxy.

---

* Corresponding author.
E-mail address: chao@uidaho.edu (C. Ma).
Peer-review under responsibility of China University of Geosciences (Beijing).

https://doi.org/10.1016/j.gsf.2020.01.013
Received 28 June 2019; Received in revised form 2 December 2019; Accepted 26 January 2020

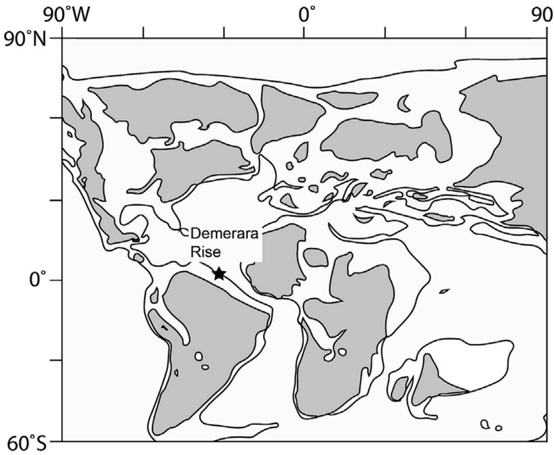

Fig. 1. Paleogeographic map for the Late Cretaceous (90 Ma) (modified from Ron Blakey http://jan.ucc.nau.edu/rcb7/ and the Colorado Plateau Geosystems Inc.). Black star shows the location of ODP Site 1259, Demerara Rise.

Paleoclimate proxies may have different response to astronomical forcing and non-astronomical noise (Li et al., 2019; Ma et al., 2019). For example, some proxies (e.g., grayscale) may have a linear relationship with $CaCO_3$ content (Eldrett et al., 2015a) while other proxies may have a logarithm relationship (Locklair and Sageman, 2008). Some proxies may be dominated by astronomical forcing while other proxies may be largely influenced by non-orbital noise. Consequently, astronomical time scale constructed from a single proxy may have uncertainty that cannot be fully assessed.

Testing multiple paleoclimate proxies may solve this problem especially at geological records where the preservation of paleoclimate signals is complicated. Recognition of astronomical forcing in variations of rock properties from Site 1259 of Cretaceous Demerara Rise in the equatorial Atlantic of 85–94 Ma is not straightforward: color reflection, bulk density and natural gamma radiation (NGR) that reflect clay content in the Demerara Rise do not correlate linearly (Supplemental Fig. S1). For a full assessment of the uncertainty of astronomical time scale from multiple proxies, we applied two astrochronological methods to four paleoclimate proxies and constructed an astronomical time scale for the Turonian throughout Coniacian at the Demerara Rise (85–94 Ma). The result compares with previous studies within error and provides insight into the uncertainties in astronomical time scales.

2. Material and method

2.1. Material

Submarine plateau of the Demerara Rise is located at about 5°N off the coasts of Surinam and French Guyana (Fig. 1; Erbacher et al., 2004). Five sites (1257–1261) of ODP Leg 207 have recovered Cretaceous sediments from the Albian to the Campanian. Among these, the most complete stratigraphy at Site 1259 (GPS: 9°18′N, 54°12′W) records one of major global carbon perturbation events, known as Oceanic Anoxic Event 2 (OAE2) and its aftermath (Erbacher et al., 2004). Sediments of the Turonian throughout the Coniacian at Site 1259 are mainly laminated black shale interbedded with carbonate-rich shale (Fig. 2).

Site 1259 has three holes: A, B, and C, all of which have their own depth in meters below seafloor (mbsf) that can be converted to meters composite depth (mcd). Here we converted all depth to mbsf of Hole A based on the converting table by Erbacher et al. (2004) because Hole A is the most complete and widely used profile (Erbacher et al., 2005). Data in depth converting table (Erbacher et al., 2004) were used as tie points and the depths between these tie points were linearly interpolated. Data from Hole B and C were converted to the mbsf of Hole A, thus data from Hole A, B, and C were composed to new data that cover most of the studied interval (Fig. 2).

Biostratigraphy of calcareous nannofossils (Hardas and Mutterlose, 2006; Bornemann et al., 2008) and chemostratigraphy (Erbacher et al., 2005) have been studied at Site 1259, which was utilized as a preliminary time frame for this cyclostratigraphic investigation. Accordingly, the Cenomanian/Turonian (C/T) boundary is between the first occurrence (FO) of the calcareous nannofossil *Q. Intermedium* at 545.40 m and the FO of *E. octopetalus* at 544.70 m of Site 1259, and the C/T boundary is closer to the FO of *Q. Intermedium* (545.4 m of Site 1259) (Erbacher et al., 2005; Hardas and Mutterlose, 2006; Bornemann et al., 2008). Thus, the depth of the C/T boundary is between 545.40 m and 545.05 m (the middle of two above FOs). We assigned the C/T boundary at 545.23 m, the mid-point between 545.40 m and 545.05 m. The standard deviation (*SD*) of the depth of C/T boundary is defined based on the standard deviation of uniform distribution as

$$SD = \sqrt{\frac{(D_2 - D_1)^2}{12}} \tag{1}$$

where D_2 is the lower FO (545.40 m) and D_1 is the upper FO (545.05 m). Therefore, the *SD* is 0.10 m in this case. The Turonian/Coniacian boundary is defined by the FO of *M. furcatus* (CC12/CC13) at 512.45 mcd (Bornemann et al., 2008), which is equivalent to 510.7 mbsf (Erbacher et al., 2004). The Coniacian/Santonian boundary is constrained between FO of *L. grillii* (499.3 mcd) and FO of *M. decussata* (501.2 mcd) (Bornemann et al., 2008), which is between 497.55 m and 499.45 m (Erbacher et al., 2004). Thus, following the method above, the position for the Coniacian/Santonian boundary is 498.50 m with a standard deviation of 0.55 m. Calcareous nannofossil zones investigated in this study are the base of CC12 (CC11/CC12), the base of CC13 (CC12/CC13) and the base of CC14 (CC13/CC14), which correspond to depths of 521.51 mcd (519.76 mbsf), 512.45 mcd (510.7 mbsf), and 501.2 mcd (499.50 mbsf), respectively. Because no ash beds were found in this interval at Demerara Rise, the Cenomanian/Turonian boundary (93.9 ± 0.15 Ma, Meyers et al., 2012) in the Western Interior Basin, USA was chosen as the anchor for our ATS.

Multiple paleoclimate proxies are from IODP Log Processing and Database (Erbacher et al., 2004) for Site 1259, including color reflection L* and b*, natural gamma radiation (NGR), and bulk density. These four proxies were used because they either have been proven carrying astronomical signals in the mid-Cretaceous of the Demerara Rise (e.g., L* and b*, Nederbragt et al., 2007) or have great potential to carry astronomical signals (e.g., density and gamma radiation, Li et al., 2019). Details of measurement methods for these proxies can be seen in Blum (1997). Rock color can be digitalized using a three-dimension color model such as the CIE LAB (L*, a*, and b*) color system (Robertson, 1977; Li et al., 2019). L* denotes lightness reflecting the richness of calcium carbonate, which is primarily influenced by carbonate productivity (Eldrett et al., 2015a, b). b* represents yellowness (positive values for yellow and negative values for blue), which may reflect iron-bearing minerals and bottom-water redox conditions (Li et al., 2019). These two proxies have been proven carrying astronomical signals in the Demerara Rise (Nederbragt et al., 2007). Changes in NGR and density in marine sediments represent variations in clay content; shale-rich beds show high NGR and low density while carbonate-rich beds show low NGR and high density. These data were collected from 497.25 mbsf to 550.48 mbsf, with a sampling resolution of 0.025 m.

2.2. Time series analysis

This study applied a set of quantitative and statistical methods in time series analysis. Multi-taper method (MTM, Thomas, 1982) power spectral analysis and F-test evaluation were used to identify significant frequencies in paleoclimate proxies. Evolutive harmonic analysis (EHA) was performed to track spatial frequencies that are associated with

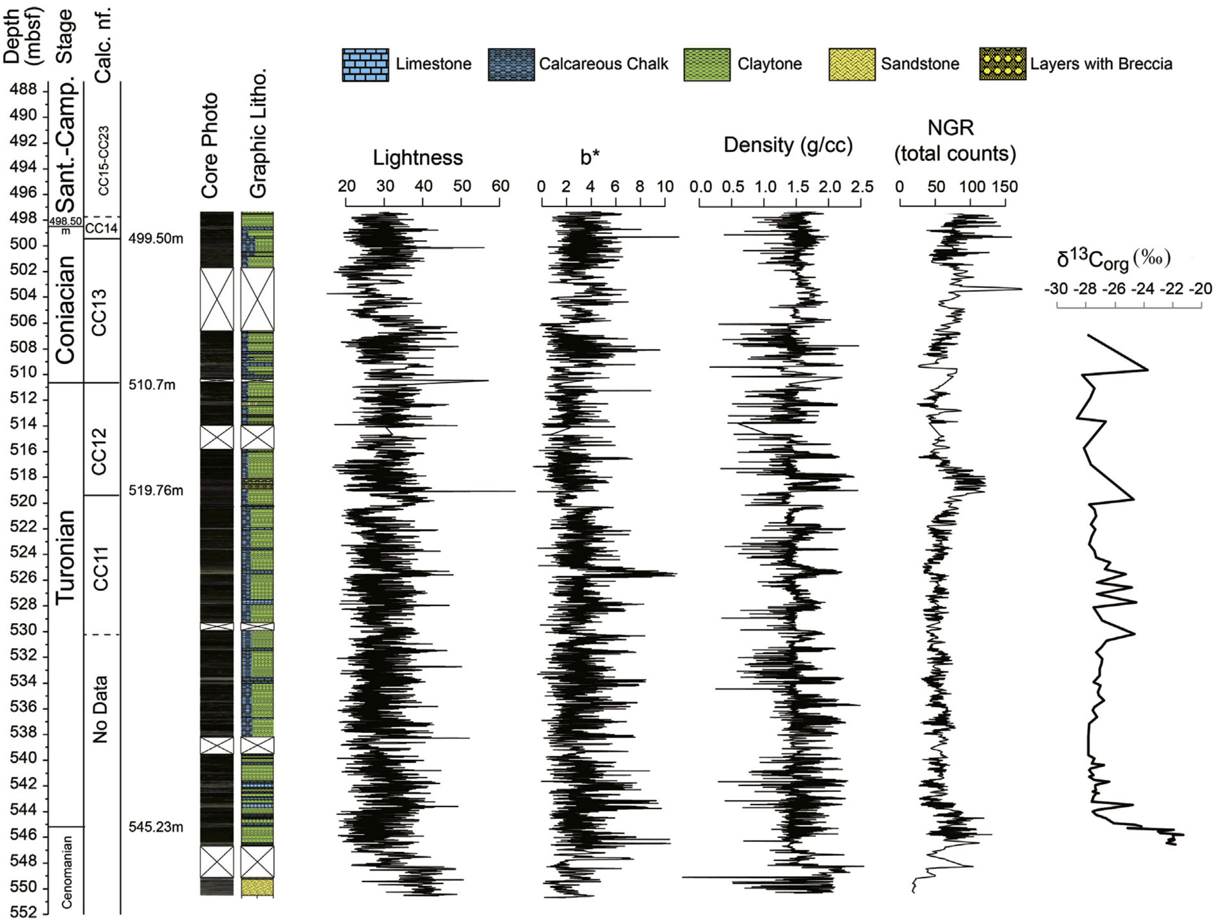

Fig. 2. Stratigraphy, lithology, and proxy data at Site 1259. Biozones are from Bornemann et al. (2008). Data of Lightness, b*, density and NGR (natural gamma radiation) are from Erbacher et al. (2004) and $\delta^{13}C_{org}$ are from Erbacher et al. (2005). Sant.–Santonian. Camp.–Campanian. Calc. nf.–Calcareous nanofossils. Litho.–lithology.

astronomical frequencies with moving-window MTM analysis, which is to track variations of the sedimentation rates (Meyers et al., 2001; Ma et al., 2014; Eldrett et al., 2015a). Average spectral misfit (ASM, Meyers et al., 2007) was used to search for the optimal sedimentation rate via fitting the spatial frequencies to orbital frequencies and the null hypothesis of no astronomical forcing was tested with Monte Carlo realizations. To evaluate age models derived from different astrochronological techniques, we adopted two methods of constructing astronomical time scale based on the most stable long eccentricity cycle (Laskar et al., 2004): (1) time calibration using bandpass filtering of the recognized long eccentricity cycles (E1 bandpass, Li et al., 2016; Wu et al., 2018) and (2) tracking the long eccentricity from the EHA result (tracking EHA, Ma et al., 2017). Linearly detrending was first conducted to L*, b*, density, and NGR series. Then the EHA method was applied to the four datasets, with a moving window of 5 m and a step of 0.1 m (Fig. 3). Sedimentation rates were derived by tracking significant long eccentricity signal from EHA manually based on frequencies that are higher than 80% F-test probability (bottom panels in Fig. 3) and consistent with the long eccentricity frequencies identified from ASM results (Table 2). In the E1 bandpass method, long eccentricity cycles were extracted by using Gaussian bandpass filter from the four proxies based on the frequencies identified in ASM. All these analyses were performed using "*astrochron*" package in R (Meyers, 2014).

3. Results

3.1. Time series analysis

Strong and straight frequency peaks revealed in EHA plots suggest a relatively stable sedimentation rate (cf. Meyers et al., 2001). Based on characteristics of the EHA plots, the datasets were divided into four intervals (see black and white boxes in Fig. 3) to perform MTM power spectral analysis for the extraction of significant frequencies. These four intervals were: 497.25–510 m, 510–520 m, 520–530 m, and 530–550.48 m. Because of the different stability of frequencies in the EHA result of L*, the actual intervals from 510 m to 530 m in the ASM tests for L* were 510–517 m and 517–530 m (Fig. 3, Table 2 and Supplementary Figs. S1–S17). Significant frequencies passing the F-test with confidence level of ≥80%–95% (except the interval of 510–520 m for the NGR, where an F-test confidence level of ≥75% was used, Supplementary Materials) were tested with the ASM method. The null hypothesis of no astronomical forcing (H_0) and the value of sedimentation rates were evaluated. The null hypothesis test in the ASM of all four intervals in the four proxies demonstrated that astronomical forcing had a significant impact on the paleoclimate proxies (see Supplementary Figs. S1–S17). There is only one ASM test of the interval (497.25–510 m) for NGR that did not reject the null hypothesis. Sedimentation rates for the four intervals from the four

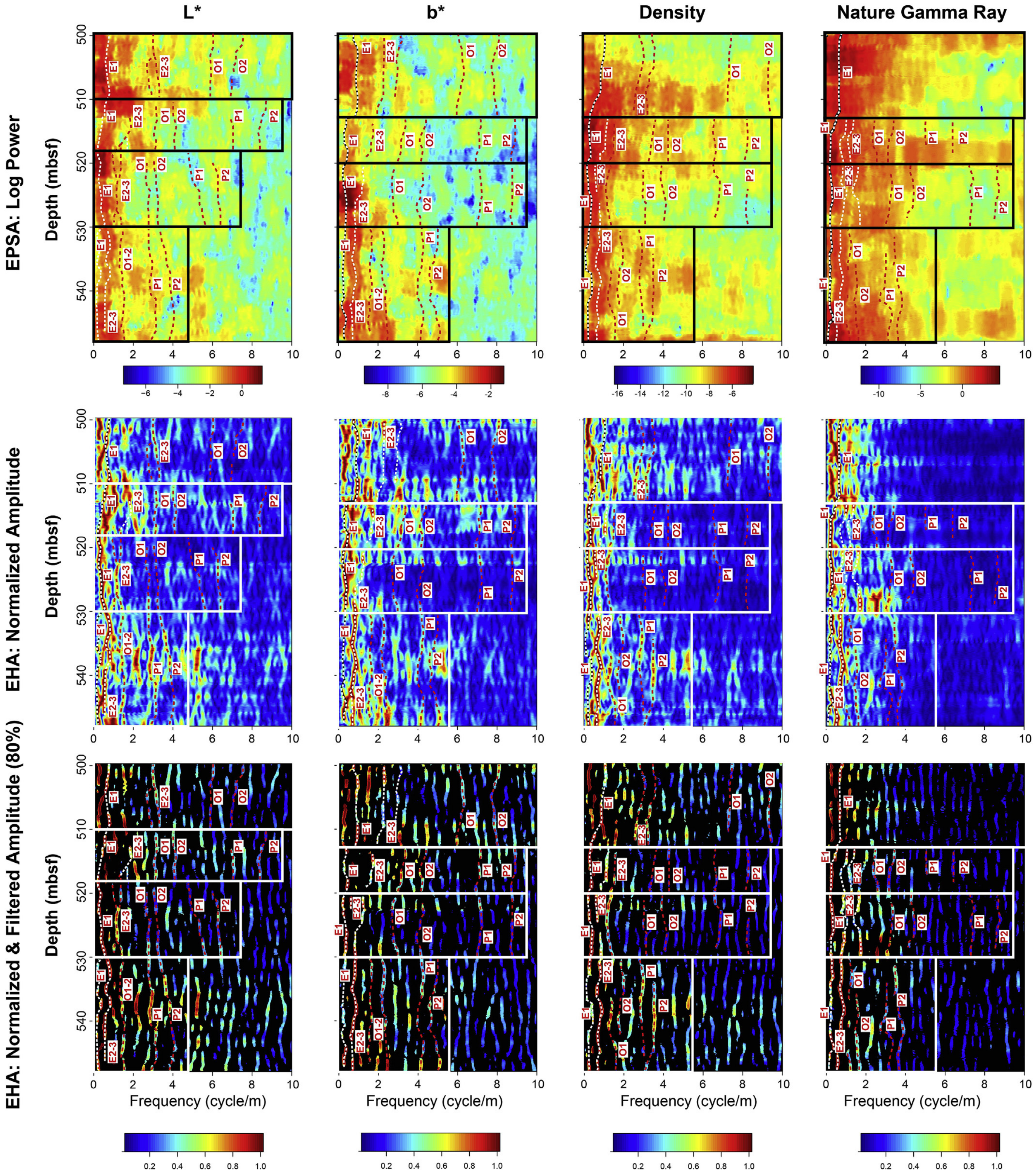

Fig. 3. EHA results for L* (first column), b* (second column), density (third column), and NGR (fourth column). The first row of the plots shows evolutive power spectral analysis (EPSA) in log power. The second row shows the normalized amplitude of EHA. The third row shows the normalized, filtered amplitude (80%) of EHA. The colored bars at the bottom for the second and third rows are the same. Red and white dotted lines indicate the trace of orbital frequencies, which are labeled with E1 (long eccentricity), E2-3 (short eccentricity), O1 (long obliquity), O2 (short obliquity), P1 (long precession), and P2 (short precession). The black (top row) and white (middle and bottom rows) boxes are the four intervals for separate ASM analyses.

Table 1
Sedimentation rates obtained from the ASM test.

Interval (m)	Sedimentation rate (cm/kyr)	Interval (m)	Sedimentation rate (cm/kyr)		
	L*		b*	Density	NGR
497.25–510	0.35	497.25–510	0.34	0.28	
510–517	0.64	510–520	0.65	0.70	0.85
517–530	0.78	520–530	0.63	0.66	0.60
530–550.48	1.43	530–550.48	1.10	1.53	1.50

proxies are listed in Table 1. By applying the sedimentation rates, astronomical cyclicities are listed in Table 2, based on which the astronomical signals were tracked on EHA results (red or white dashed lines in Fig. 3). The ASM results also guided the long eccentricity bandpass. The bandpass ranges of the four intervals of 497.25–510 m, 510–520 m, 520–530 m, and 530–550.48 m are 0.7–0.9 cycle/m, 0.18–0.55 cycle/m, 0.24–0.47 cycle/m, and 0.07–0.29 cycle/m, respectively.

3.2. *Construction of ATS and its uncertainty*

405 kyr long eccentricity cycle is considered as the most stable astronomical cycle in Earth's history (Laskar et al., 2004; Ma et al., 2017; Hinnov, 2018), therefore, long eccentricity cycle was used for the construction of the ATS in this study. According to the ASM results (Tables 1 and 2), long eccentricity cycles tracked from the EHA results (Fig. 3) and long eccentricity bandpass were utilized for determining the sedimentation rate (Fig. 4). Sedimentation rates ranged from 2 to 0.2 cm/kyr at Site 1269 from the Turonian to the Coniacian. Sedimentation rates were relatively high (0.8–2 cm/kyr) in the early Turonian, then reached to a regional low sedimentation rate at around 0.5–1 cm/kyr during the middle Turonian. It returned ~1 cm/kyr during the latest Turonian and decreased to a relatively low rate of ~0.3 cm/kyr during the Coniacian. Floating ATS was built by applying the sedimentation rates to each proxy. Finally, the absolute astronomical time scales of the four proxies were constructed by pinning the floating ATS to the Cenomanian/Turonian (C/T) boundary of 93.9 ± 0.15 Ma (Fig. 4).

The ATS enabled the determination of the mean and uncertainty of ages for stage and biozone boundaries of the Turonian–Coniacian interval (Table 3). Age models for the two methods (tracking EHA and E1 bandpass) were calculated separately. Statistical mean and standard deviation were calculated based on the four age models in each method (Table 3). We considered two sources of uncertainties: one was from ATS itself and the other one was from the anchor. Quadrature method was applied to combine uncertainties from the four age models in each method and a 0.15-Myr uncertainty of the anchor. The total uncertainty was calculated by taking the square root of the sum of the variance from all sources. For example, the age for the Turonian/Coniacian boundary is 89.74 ± 0.35 Ma based on four astrochronologies in the tracking EHA method (Table 3). Considering an 0.15-Myr uncertainty of the anchor, the total uncertainty is 0.38 Myr [obtained from sqrt(0.15×0.15 + 0.35×0.35)]. Thus, ages for the boundaries of CC11/CC12, Turonian/Coniacian (CC12/CC13), CC13/CC14, and Coniacian/Santonian are 91.17 ± 0.36 Ma, 89.74 ± 0.38 Ma, 86.13 ± 1.31 Ma, and 85.80 ± 1.33 Ma, respectively from tracking EHA method, comparing with 91.25 ± 0.20 Ma, 89.87 ± 0.20 Ma, 86.36 ± 0.33 Ma, and 86.03 ± 0.32 Ma based on E1 bandpass method (Table 3).

4. Discussion

4.1. *Comparison with previous age models*

The consistency between key boundary ages in previous studies and our results demonstrates that our methods of estimating age model and uncertainties from multiple proxies are robust. The age of Turonian/Coniacian boundary (TCB, which is equivalent to CC12/CC13 boundary) is constrained to 89.74 ± 0.41 Ma by integrating biostratigraphy, radioisotopic geochronology, and cyclostratigraphy in Sageman et al. (2014). Eldrett et al. (2015a) applied similar methods as those used in Sageman et al. (2014) but on a different sedimentary record. They obtained the age for the TCB is 89.72 ± 0.17 Ma. The radioisotopic ages used as anchors in Eldrett et al. (2015a) are from the ash beds in the studied core itself. In comparison, ages of ash beds in Sageman et al.

Table 2
Astronomically forced frequency (E1: long eccentricity, E2 and E3: short eccentricity, O1 and O2: obliquity, P1 and P2: precession).

Astronomical parameter	Astronomically forced frequencies (cycle/m)					
	Depth (m)	L*	Depth (m)	b*	Density	NGR
E1	497.25–510	0.75	497.25–510	0.84	0.85	
E2		2.20		2.19	2.80	
E3		3.03		3.02	3.60	
O1		5.75		5.98	7.40	
O2		7.64		7.75	9.30	
P1		12.66		12.99	15.83	
P2		15.46		16.06	19.18	
E1	510–517	0.50	510–520	0.37	0.38	0.23
E2		1.09		1.33	1.17	1.09
E3		1.83		1.66	1.50	1.27
O1		3.12		3.08	2.94	2.39
O2		4.09		4.03	3.89	3.12
P1		7.09		6.84	6.38	5.22
P2		8.40		8.10	7.82	6.46
E1	517–530	0.37	520–530	0.37	0.36	0.34
E2		1.12		1.23	1.19	1.41
E3		1.36		1.60	1.61	1.71
O1		2.72		3.10	3.05	3.34
O2		3.31		4.23	4.21	4.39
P1		5.67		7.18	6.85	7.39
P2		6.87		8.66	8.29	9.16
E1	530–550.48	0.17	530–550.48	0.24	0.16	0.12
E2		0.51		0.75	0.52	null
E3		0.74		0.93	0.75	0.75
O1		1.39		1.81	1.40	1.40
O2		1.87		2.39	1.70	1.56
P1		3.09		4.05	2.92	3.02
P2		3.84		4.97	3.52	3.61

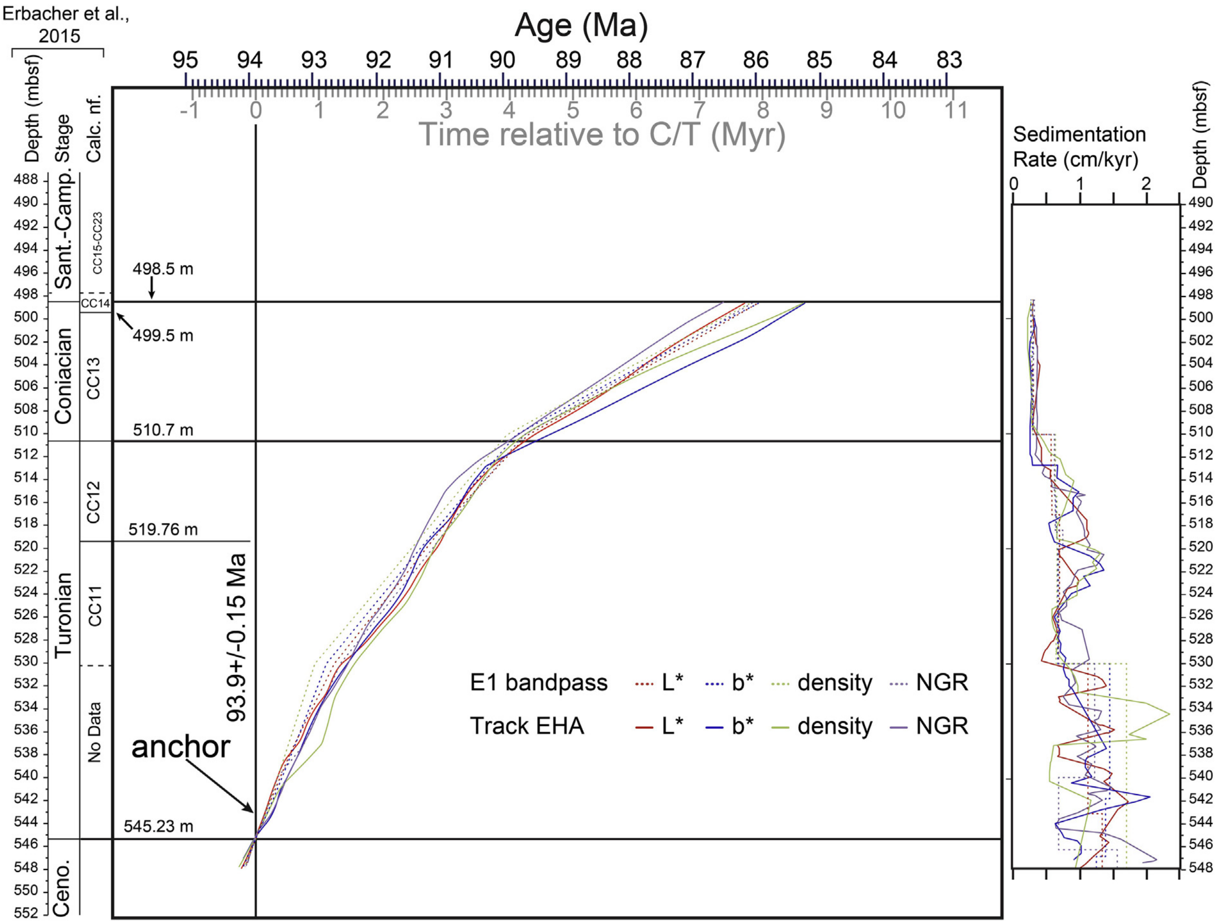

Fig. 4. Age models and sedimentation rate histories. Age models using both tracking EHA and E1 bandpass methods were based on four proxies of L* (red), b* (blue), NGR (purple), and density (light green) proxies.

(2014) are from the stratigraphic-correlated outcrop. This is one reason that the TCB age in Eldrett et al. (2015a) has smaller uncertainty. These two previous ages match well with the age of the same boundary obtained in our study: 89.74 ± 0.38 Ma from the tracking EHA method and 89.87 ± 0.20 Ma based on the E1 bandpass method. The age for the Coniacian/Santonian boundary (CSB) is 86.49 ± 0.44 Ma in Sageman et al. (2014), which is within the range of the 85.80 ± 1.33 Ma based on the tracking EHA method and 86.03 ± 0.32 Ma from the E1 bandpass method in our study.

However, there are also some inconsistencies in the age models between previous work and this study. The age for the C11/C12 boundary was constrained as 93.11 ± 0.17 Ma in Eldrett et al. (2015a), which is ~2 Ma older than the age of 91.17 ± 0.32 Ma from the tracking EHA method and 91.25 ± 0.20 Ma based on the E1 bandpass method in our study. The CC12/CC13 boundary was used as an indicator of the TCB at the Cretaceous Demerara Rise (Bornneman et al., 2008). Recent work suggests that the TCB in Texas may occur near the middle of the CC13 biozone (Corbett et al., 2014). The Turonian/Coniacian boundary is defined by the base of the *Scaphites preventricosus* ammonite biozone, which is coincident with the CC14/CC13 boundary (Gradstein et al., 2012). These suggest that calcareous nannofossil biostratigraphy may not be as stable as ammonite biostratigraphy for the age model construction in the Upper Cretaceous.

Our age model is different from a previous study at the same core (Jones et al., 2018). They constructed an age model for the stratigraphy of core 1259A from 508 m to 530 m of Site 1259 based on

Table 3
Age for stage and biozone boundaries.

Boundaries	Age Models (Ma)					Mean (Ma)	Age Model Uncertainty[b] (2σ) (Ma)	Total Uncertainty[c] (Ma)	Age (Ma) (from Sageman et al., 2014)	Age (Ma) (from Eldrett et al., 2015a)
	Models[a]	L*	b*	Density	NGR					
CC11/CC12	A	91.02	91.23	91.06	91.37	91.17	0.32	0.36	No data	93.11 ± 0.17
	B	91.19	91.28	91.42	91.09	91.25	0.13	0.20		
Turonian/Coniacian (CC12/CC13)	A	89.68	89.53	89.82	89.94	89.74	0.35	0.38	89.74 ± 0.41	89.72 ± 0.17
	B	89.73	89.90	90.05	89.78	89.87	0.13	0.20		
CC13/CC14	A	86.49	85.53	85.64	86.87	86.13	1.31	1.31	No data	No data
	B	86.30	86.33	86.44	86.38	86.36	0.29	0.33		
Coniacian/Santonian	A	86.18	85.23	85.25	86.54	85.80	1.33	1.33	86.49 ± 0.44	No data
	B	85.98	85.97	86.11	86.08	86.03	0.28	0.32		

[a] A. Tracking EHA method; B. E1 bandpass method.
[b] Uncertainty (2σ) from different age models based on different proxies.
[c] Total uncertainty derived by adding age model uncertainty and anchor (C/T boundary) uncertainty in quadrature.

cyclostratigraphy of calcium carbonate data and chemostratigraphy of carbon isotope (Supplementary Fig. S2). Their depth unit is meter composite depth (mcd), which is ~1.75 m deeper than mbsf of Hole A in our study. The sedimentation rate model by Jones et al. (2018) has a substantial difference from 512 mbsf to 520 mbsf, which is ~0.2 cm/kyr, while the sedimentation rate in our study is 0.64–0.85 cm/kyr. Other than this interval, sedimentation rate models in these two studies are similar (Supplementary Fig. S2). Because there is no anchor in their age model at Site 1259, we align two extreme age models based on their floating astronomical time scale to our age models (Supplementary Fig. S2). The age model of Jones et al. (2018) (left light blue curve in Supplementary Fig. S2) assigns a 100–200 kyr duration to the interval from 528 mbsf to 545 mbsf at Site 1259, which implies that the sedimentation rate for this interval is 8.5–17 cm/kyr, an unreasonable range for the shale deposition of this interval at Demerara Rise. Another scenario (right light blue curve in Supplementary Fig. S2) would make the TCB be 88.6 Ma, which is 1000 kyr younger than previous studies (Sageman et al., 2014; Eldrett et al., 2015a). Consequently, we argue that our age model is more practical.

4.2. *Signal and noise evaluation*

In cyclostratigraphic study, the signal usually refers to astronomical-related climate oscillations (i.e., eccentricity, obliquity, and precession cycles) while the noise frequently refers to the residual oscillations or non-orbital related components. In a statistical sense, ASM results and sedimentation rate histories from all four proxies in both methods of E1 bandpass and tracking EHA are similar along with the record (Tables 1 and 2, Fig. 4). All of them indicate that these proxy oscillations are of the astronomical origin at Site 1259 of the Demerara Rise. For the L* within the interval of 510 m to 530 m, subdivision for ASM tests is different from the other three proxies. And the ASM-derived sedimentation rates of the L* series at the 520–530 m interval are higher than those derived from the other three proxies. This may be caused by the low signal-to-noise ratio in the L* record, which could reduce the relative power of astronomical signals at this interval. Proxy's oscillations during the Coniacian may have a low signal-to-noise ratio, indicated by no reliable ASM result in the NGR data (Table 2). Different proxies in the same stratigraphy display different degrees of signal-to-noise ratio; even in some intervals, a specified proxy may not preserve strong astronomical signals due to strong noise. In a few intervals of a specified proxy in this study, identified astronomical cycles have lower confidence levels. For instance, the confidence level (CL) of filtering spatial frequencies that were analyzed in ASM for NGR within the interval of 510–520 m is 75%, while the CLs of the similar spatial frequencies in L*, b* and density are 90%, 80%, and 90% respectively. We can imagine that if only NGR was used in this interval, the result may be questionable because of the high probability of false-positive frequencies.

Sources of noise in paleoclimate oscillations fall into two categories: syndepositional noise and postdepositional noise. The syndepositional noise happens during the depositional processes, including basinal uplift/subsidence, volcanic eruptions, earthquakes, and autogenic processes, among others (Li et al., 2018). These noises could be recorded in most of the proxies that display comparable noise profiles. For example, ash beds should be removed from all proxies before the evaluation of astronomical signals. Postdepositional noise includes sources from bioturbation, compaction, and diagenesis that take place after the deposition of sediments (Weedon, 2003). Various types of diagenesis (e.g., oxygenation and remineralization) may affect different proxies in sedimentary rocks. The L* that reflects the carbonate versus organic matter may be affected by the remineralization of carbonate. The b* that reflects iron-bearing minerals and bottom water redox conditions could also be affected by the redox conditions after deposition (Li et al., 2019). Three main sources of natural gamma radiation are radiogenic isotopes of potassium (K), uranium (U) and thorium (Th) (Ruffelll and Worden, 2000). Post-depositional migration of organic matter could affect the radiogenic source of U, thus natural gamma radiation (Li et al., 2019). Bulk density indicates changes in lithology and porosity (Blum, 1997). Post-depositional processes such as different compaction and mineral alternation lead to elevated "noise" in density data.

Taken together, cyclostratigrapher should be careful when conducting cyclostratigraphic studies based on a single proxy. Identifying the same astronomical cycles from multiple proxies in the same strata is shown here to be a practical way to overcome the risks of low signal-to-noise ratio and false-positive frequencies identified as astronomical signals.

4.3. *Challenges and opportunities of our methods*

There are two main methods of constructing an astronomical time scale for deep time beyond 50 Ma: tracking a specific orbital frequency from the EHA method (Eldrett et al., 2015; Ma et al., 2017) and bandpass filtering of a specific orbital cycle (Li et al., 2016; Wu et al., 2018). Both have their own limitations. Paleoclimate proxies are not only influenced by astronomical forcing, non-astronomical forcing may lead to very low signal-to-noise ratio, which has influences on both tracking EHA and bandpass methods. The tracking EHA method has subjective uncertainties in tracking frequencies from the EHA plot: (1) it is manually tracked and (2) the tracked frequencies must be larger than a given confidence level. Clearly, this method subjectively introduces uncertainties to the construction of sedimentation rates and age models. Cyclostratigraphers have to make choices of tracked frequency peaks based on their experience. This uncertainty is impossible to quantify when only one proxy data is used. In comparison, approaches of the bandpass filtering have subjective uncertainties as well (Sinnesael et al., 2019). There are no universally accepted choices of frequency bands for the filtering of a specific astronomical signal (Zeeden et al., 2018). Different filtering settings, which usually depend on cyclostratigraphers' decision, may result in different age models. In sum, the subjective uncertainties in both methods are affected by the knowledge and experience of the cyclostratigrapher (Sinnesael et al., 2019).

5. Conclusion

Consistency of time series analyses on four proxies (L*, b*, density, and NGR) using two methods (tracking EHA and E1 bandpass methods) demonstrates the existence of astronomical forcing during the Turonian throughout the Santonian at the Demerara Rise in the equatorial Atlantic. Results of the astronomical time scale based on four proxies in both methods are different, demonstrating different paleoclimate proxies may preserve different signal-to-noise ratios in the aspect of astronomical forcing. This issue can be addressed from the statistical uncertainty of these astronomical time scales based on four proxies in both methods. The final uncertainty of the astronomical time scales was obtained by the quadrature algorithm applied to uncertainties from proxies and uncertainty from the anchor. The calibrated ages of the boundaries of CC11/CC12, Turonian/Coniacian (CC12/CC13), CC13/CC14 and Coniacian/Santonian compare well with previous studies (Sageman et al., 2014; Eldrett et al., 2015a). Future works could be quantifying non-astronomical noises in different paleoclimate proxies.

Declaration of competing interest

The authors declare that they have no known competing financial interests or personal relationships that could have appeared to influence the work reported in this paper.

Acknowledgement

We thank James Eldrett and Stephen R. Meyers for their discussions. We also thank two anonymous reviewers for their constructive comments that improved this paper. This study was supported by NSF CAREER award to Stephen R. Meyers (EAR-1151438) and partially supported by the NSF Grant with No. 1835717.

Appendix A. Supplementary data

Supplementary data to this article can be found online at https://doi.org/10.1016/j.gsf.2020.01.013.

References

Blum, P., 1997. Physical properties handbook. In: ODP Tech. Note, 26. https://doi.org/10.2973/odp.tn.26.1997.

Bornemann, A., Norris, R.D., Friedrich, O., Beckmann, B., Schouten, S., Damsté, J.S.S., Vogel, J., Hofmann, P., Wagner, T., 2008. Isotopic evidence for glaciation during the Cretaceous supergreenhouse. Science 319 (5860), 189–192.

Corbett, M.J., Watkins, D.K., Pospichal, J.J., 2014. A quantitative analysis of calcareous nannofossil bioevents of the Late Cretaceous (Late Cenomanian–Coniacian) Western Interior Seaway and their reliability in established zonation schemes. Mar. Micropaleontol. 109, 30–45.

De Vleeschouwer, D., Parnell, A.C., 2014. Reducing time-scale uncertainty for the Devonian by integrating astrochronology and Bayesian statistics. Geology 42 (6), 491–494.

Eldrett, J.S., Ma, C., Bergman, S.C., Lutz, B., Gregory, F.J., Dodsworth, P., Phipps, M., Hardas, P., Minisini, D., Ozkan, A., Ramezani, J., 2015a. An astronomically calibrated stratigraphy of the Cenomanian, Turonian and earliest Coniacian from the Cretaceous Western Interior Seaway, USA: implications for global chronostratigraphy. Cretac. Res. 56, 316–344.

Eldrett, J.S., Ma, C., Bergman, S.C., Ozkan, A., Minisini, D., Lutz, B., Jackett, S.J., Macaulay, C., Kelly, A.E., 2015b. Origin of limestone–marlstone cycles: astronomic forcing of organic-rich sedimentary rocks from the Cenomanian to early Coniacian of the Cretaceous Western Interior Seaway, USA. Earth Planet Sci. Lett. 423, 98–113.

Erbacher, J., Friedrich, O., Wilson, P.A., Birch, H., Mutterlose, J., 2005. Stable organic carbon isotope stratigraphy across oceanic anoxic event 2 of Demerara Rise, western tropical Atlantic. Geochemistry, Geophysics, Geosystems 6 (6). https://doi.org/10.1029/2004GC000850.

Erbacher, J., Mosher, D.C., Malone, M.J., Sexton, P., Wilson, P.A., 2004. Proc. ODP, Init. Repts., vol 207. Ocean Drilling Program, College Station, TX. https://doi.org/10.2973/odp.proc.ir.207.2004.

Gradstein, F.M., Ogg, J.G., Schmitz, M.D., Ogg, G., 2012. The Geologic Time Scale 2012. Elsevier, Amsterdam, p. 1144.

Hardas, P., Mutterlose, J., 2006. Calcareous nannofossil biostratigraphy of the Cenomanian/Turonian boundary interval of ODP Leg 207 at the Demerara Rise. Rev. Micropaleontol. 49 (3), 165–179.

Hinnov, L.A., 2018. Cyclostratigraphy and astrochronology in 2018. In: Montenari, M. (Ed.), Cyclostratigraphy and Astrochronology. Stratigraphy & Timescales 3, pp. 1–80.

Jones, M.M., Sageman, B.B., Meyers, S.R., 2018. Turonian sea level and paleoclimatic events in astronomically tuned records from the tropical north Atlantic and western interior seaway. Paleoceanogr. Paleoclimatol. 33 (5), 470–492.

Kuiper, K.F., Deino, A., Hilgen, F.J., Krijgsman, W., Renne, P.R., Wijbrans, A.J., 2008. Synchronizing rock clocks of Earth history. Science 320 (5875), 500–504.

Laskar, J., Robutel, P., Joutel, F., Gastineau, M., Correia, A.C.M., Levrard, B., 2004. A long-term numerical solution for the insolation quantities of the Earth. Astron. Astrophys. 428 (1), 261–285.

Li, M., Ogg, J., Zhang, Y., Huang, C., Hinnov, L., Chen, Z.-Q., Zou, Z., 2016. Astronomical tuning of the end-Permian extinction and the Early Triassic Epoch of South China and Germany. Earth Planet Sci. Lett. 441, 10–25.

Li, M., Hinnov, L.A., Huang, C., Ogg, J.G., 2018. Sedimentary noise and sea levels linked to land–ocean water exchange and obliquity forcing. Nat. Commun. 9, 1004. https://doi.org/10.1038/s41467-018-03454-y.

Li, M., Huang, C., Ogg, J., Zhang, Y., Hinnov, L., Wu, H., Chen, Z.Q., Zou, Z., 2019. Paleoclimate proxies for cyclostratigraphy: comparative analysis using a Lower Triassic marine section in South China. Earth Sci. Rev. 189, 125–146.

Locklair, R.E., Sageman, B.B., 2008. Cyclostratigraphy of the Upper Cretaceous Niobrara Formation, western interior, USA: a Coniacian–Santonian orbital timescale. Earth Planet Sci. Lett. 269 (3–4), 540–553.

Ma, C., Meyers, S.R., Sageman, B.B., 2019. Testing Late Cretaceous astronomical solutions in a 15 million year astrochronologic record from North America. Earth Planet Sci. Lett. 513, 1–11.

Ma, C., Meyers, S.R., Sageman, B.B., 2017a. Theory of chaotic orbital variations confirmed by Cretaceous geological evidence. Nature 542 (7642), 468.

Ma, C., Meyers, S.R., Sageman, B.B., Singer, B.S., Jicha, B.R., 2014. Testing the astronomical time scale for oceanic anoxic event 2, and its extension into Cenomanian strata of the Western Interior Basin (USA). Geol. Soc. Am. Bull. 126 (7–8), 974–989.

Ma, P., Wang, C., Meng, J., Ma, C., Zhao, X., Li, Y., Wang, M., 2017b. Late Oligocene-early Miocene evolution of the Lunpola Basin, central Tibetan Plateau, evidences from successive lacustrine records. Gondwana Res. 48, 224–236.

Meyers, S.R., Sageman, B.B., Hinnov, L.A., 2001. Integrated quantitative stratigraphy of the Cenomanian-Turonian Bridge Creek Limestone Member using evolutive harmonic analysis and stratigraphic modeling. J. Sediment. Res. 71 (4), 628–644.

Meyers, S.R., Sageman, B.B., 2007. Quantification of deep-time orbital forcing by average spectral misfit. Am. J. Sci. 307 (5), 773–792.

Meyers, S.R., Siewert, S.E., Singer, B.S., Sageman, B.B., Condon, D.J., Obradovich, J.D., Jicha, B.R., Sawyer, D.A., 2012. Intercalibration of radioisotopic and astrochronologic time scales for the Cenomanian-Turonian boundary interval, Western Interior Basin, USA. Geology 40 (1), 7–10.

Meyers, S.R., 2014. Astrochron: An R Package for Astrochronology. https://cran.r-project.org/package=astrochron

Nederbragt, A.J., Thurow, J., Pearce, R., 2007. Sediment composition and cyclicity in the mid-Cretaceous at Demerara Rise, ODP Leg 207. In: Proceedings of the Ocean Drilling Program, Scientific Results, vol 207, pp. 1–31.

Robertson, A.R., 1977. The CIE 1976 color-difference formulae. Color Res. Appl. 2 (1), 7–11.

Ruffell, A., Worden, R., 2000. Palaeoclimate analysis using spectral gamma-ray data from the Aptian (Cretaceous) of southern England and southern France. Palaeogeogr. Palaeoclimatol. Palaeoecol. 155 (3–4), 265–283.

Sageman, B.B., Singer, B.S., Meyers, S.R., Siewert, S.E., Walaszczyk, I., Condon, D.J., Jicha, B.R., Obradovich, J.D., Sawyer, D.A., 2014. Integrating ^{40}Ar/^{39}Ar, U-Pb, and astronomical clocks in the Cretaceous Niobrara Formation, western Interior Basin, USA. Bulletin 126 (7–8), 956–973.

Sinnesael, M., De Vleeschouwer, D., Zeeden, C., Batenburg, S.J., Da Silva, A.-C., de Winter, N.J., Dinarès-Turell, J., Drury, A.J., Gambacorta, G., Hilgen, F.J., Hinnov, L.A., Hudson, A.J.L., Kemp, D.B., Lantink, M.L., Laurin, J., Li, M., Liebrand, D., Ma, C., Meyers, S.R., Monkenbusch, J., Montanari, A., Nohl, T., Pälike, H., Pas, D., Ruhl, M., Thibault, N., Vahlenkamp, M., Valero, L., Wouters, S., Wu, H., Claeys, P., 2019. The Cyclostratigraphy Intercomparison Project (CIP): consistency, merits and pitfalls. Earth Sci. Rev. 199, 102965. https://doi.org/10.1016/j.earscirev.2019.102965.

Thomson, D.J., 1982. Spectrum estimation and harmonic analysis. Proc. IEEE 70 (9), 1055–1096.

Weedon, G.P., 2003. Time Series Analysis and Cyclostratigraphy: Examining Stratigraphic Records of Environmental Cycles. Cambridge University Press.

Westerhold, T., Röhl, U., Laskar, J., 2012. Time scale controversy: accurate orbital calibration of the early Paleogene. Geochemistry, Geophysics, Geosystems 13 (6). https://doi.org/10.1029/2012GC004096.

Wu, H., Fang, Q., Wang, X., Hinnov, L.A., Qi, Y., Shen, S.Z., Yang, T., Li, H., Chen, J., Zhang, S., 2018. An 34 m.y. astronomical time scale for the uppermost Mississippian through Pennsylvanian of the Carboniferous System of the Paleo-Tethyan realm. Geology 47 (1), 83–86.

Zeeden, C., Kaboth, S., Hilgen, F.J., Laskar, J., 2018. Taner filter settings and automatic correlation optimisation for cyclostratigraphic studies. Comput. Geosci. 119, 18–28.